Stem Cell Research & Therapy

RESEARCH

Open Access

Geometrical constraints dictate assembly and phenotype of human iPSC-derived motoneuronal spheroids

Eleonora Mello[1,2], Stefano Sorrentino[1,3], Alessio Bucciarelli[4], Ermanno Cordelli[1,5], Elisa De Luca[1,6], Haakon Nygaard[3], Stefan Wendt[7], Alberto Rainer[8,9], Giuseppe Gigli[1,5], Lorenzo Moroni[10], Alessandro Polini[1] and Pamela Mozetic[1*]

Abstract

Background Neuronal spheroids represent an easy and versatile solution to model neuronal tissue in vitro. Conventional approaches to generate spheroids lack accurate size control, scalability, and customizability. This is even more exacerbated in case of pluripotent stem cell (PSC) derived spheroids, which remain challenging to standardize. Microwell devices address these limitations, providing an optimal balance between accessibility and scalability. With the aim of optimizing culture conditions, we parametrically investigated the role of microwell geometry on the formation and maturation of iPSC-derived motor neuron precursor (MNP) spheroids.

Methods We developed a customizable mold device using Digital Light Processing (DLP) 3D printing to fabricate agarose microwell arrays with distinct aspect ratios for culturing hiPSC-derived MNP spheroids with high reproducibility. We generated nine different pyramidal microwell array geometries for culturing size-controlled spheroids in the 40–140 µm diameter range. We then evaluated the differential expression of genes related to cell proliferation and motor-neuron differentiation as function of microwell geometry and spheroid size.

Results Our results indicate that spheroid size is significantly influenced by the microwell geometry, reliably due to cell partitioning at the seeding stage. Expression of proliferation and differentiation markers, such as motor neuron and pancreas homeobox 1 (MNX1) and Islet-1 (ISL1) transcription factors, is also dependent on microwell geometry and spheroid morphological descriptors.

Conclusion Our approach enables the scalable production of size-controlled MNP spheroids and underscores the effect of geometrical confinement on regulating motor neuron differentiation.

Keywords Neuronal spheroids, Motor neurons, Microwell, HiPSCs, MNX1, ISL1

Eleonora Mello and Stefano Sorrentino are co-first authors.

Alessandro Polini and Pamela Mozetic are co-last authors.

*Correspondence:
Pamela Mozetic
pamela.mozetic@nanotec.cnr.it

Full list of author information is available at the end of the article

Introduction

The human nervous system (NS) is organized in a hierarchical complex architecture where neurons and glial cells are connected in intricate functional networks. This makes the NS extremely difficult to model in vitro and only slightly reproducible with classic two-dimensional (2D) cell cultures [1]. The NS multicellular heterogeneity and the challenging accessibility and scalability of human primary cell cultures have always represented an obstacle to NS modelling redirecting the efforts on animal models for both physiological and pathological studies [2].

The advent of human induced pluripotent stem cells (hiPSCs) three-dimensional (3D) neuronal platforms, such as organoids [3], organ-on-chip [4], 3D bioprinted models [5], scaffold-based [6] and scaffold-free [7] cell cultures has marked a fundamental improvement in neurobiology [8]. The remarkable neuronal differentiative potential of iPSCs [9] combined with their almost unlimited renewal capability and non-invasive derivability from patients, has offered a new horizon for a more personalized medicine approach [10]. The 3D configuration is more effective in mimicking the brain tissue architecture, promoting more accurate cell-to-cell and cell-to-matrix interactions, and a better fluidic dynamic exchange for nutrients, oxygen, and drugs than standard 2D cultures [11, 12].

Among 3D neuronal models, spheroids appear as an easy and versatile solution [13] to better model neuronal tissue in vitro. Spheroids are self-assembled cell clusters formed by spontaneous or forced aggregation in either scaffold or scaffold-free environment [14]. Spheroids have been used to recapitulate the fundamental features of brain tissues in terms of self-organization, cell differentiation [15] electrophysiology, and neural networking in 3D [16]. Neuronal spheroids have also demonstrated useful models in the field of neurodegenerative disorders such as Alzheimer's disease [17, 18] or Amyotrophic Lateral Sclerosis [19, 20] making them suitable for high throughput [21, 22] and drug screening purposes [23, 24]. Such translational applications require high reproducibility, scalability, and adaptability, which are currently lacking in spheroids culturing methods. Conventional approaches, such as hanging drop and low-attachment cultures rely on physical stimuli, e.g., gravity or surface tension. Despite being easily accessible and reproducible, these methods give scarce control over spheroid size and can lead to heterogeneous or merged spheroids. More advanced techniques, which include microfluidic platforms, bioreactors, and magnetic manipulation involve external forces, tools, and strategies for precise control of the aggregation process [25]. While enabling more refined control and automation on spheroids development, they show limitations in terms of scalability and are difficult to be translated to non-specialized laboratories.

Microwell devices provide an optimal balance between accessibility, control outcomes, and scalability. A microwell device consists of hundreds of micrometer-sized pocket arrays capable of trapping individual cells without external force [26]. The use of microwells for tissue engineering has found increasing popularity for culturing PSC-derived spheroids with controllable size, shape, and homogeneity [27–29]. Interestingly, spatial and geometrical confinement of cells within the pocket array constitutes a regulatory stimulus for spheroid development [30–32]. While there is a relatively well-established understanding of the effect of soluble factors on spheroid formation, the contribution of mechanobiological clues remains uncertain. The influence of shape and force on cell proliferation [33], differentiation, and tissue patterning [34] has been thoroughly investigated in embryonic tissues [35]. It has been shown that differential gene expression patterns are regulated not only by morphogens but also by spatial and mechanotransduction stimuli. Considering the significant role of spatial cues in directing human embryonic development and hPSC differentiation, we hypothesized that the microwell shape might also affect spheroid development, with these changes reflected in differential gene expression. To assess the impact of geometric confinement on spheroid development, we sought to explore a parametric study to address the effect of microwell geometrical cues on the resulting MNP spheroid formation and differentiation.

Materials and methods

Materials

The complete list of chemicals, culture media and PCR primer assays used in this study is reported in Supplementary Information (Tables S1-S5).

Mold device design and fabrication

The mold design was generated using Rhinoceros software (v. 6.0, Robert McNeel & Associates). Briefly, truncated pyramids with a major base edge of 150, 400, or 800 µm, a minor base edge of 50 µm and a height of 150, 400, or 800 µm, were generated as a square array laid into a circular pocket with a diameter of 15 mm (to fit the wells of a 24-well plate) and a depth of 0.6 mm (Fig. 1A). The complete list of geometries (from g1 to g9) is reported in Table 1. Molds were fabricated by Digital Light Processing (DLP) 3D printing (MAX X27 UV, Asiga, Australia). A biocompatible resin (GR-10, Pro3Dure, Germany) was used for mold fabrication (resin details are reported in Table S2). DLP parameters were set following a previously optimized protocol [36] and the layer thickness was set at 25 µm. To characterize the pyramid geometries, a test specimen containing all 9 geometries was printed with the same DLP printing parameters and observed under a Field Emission

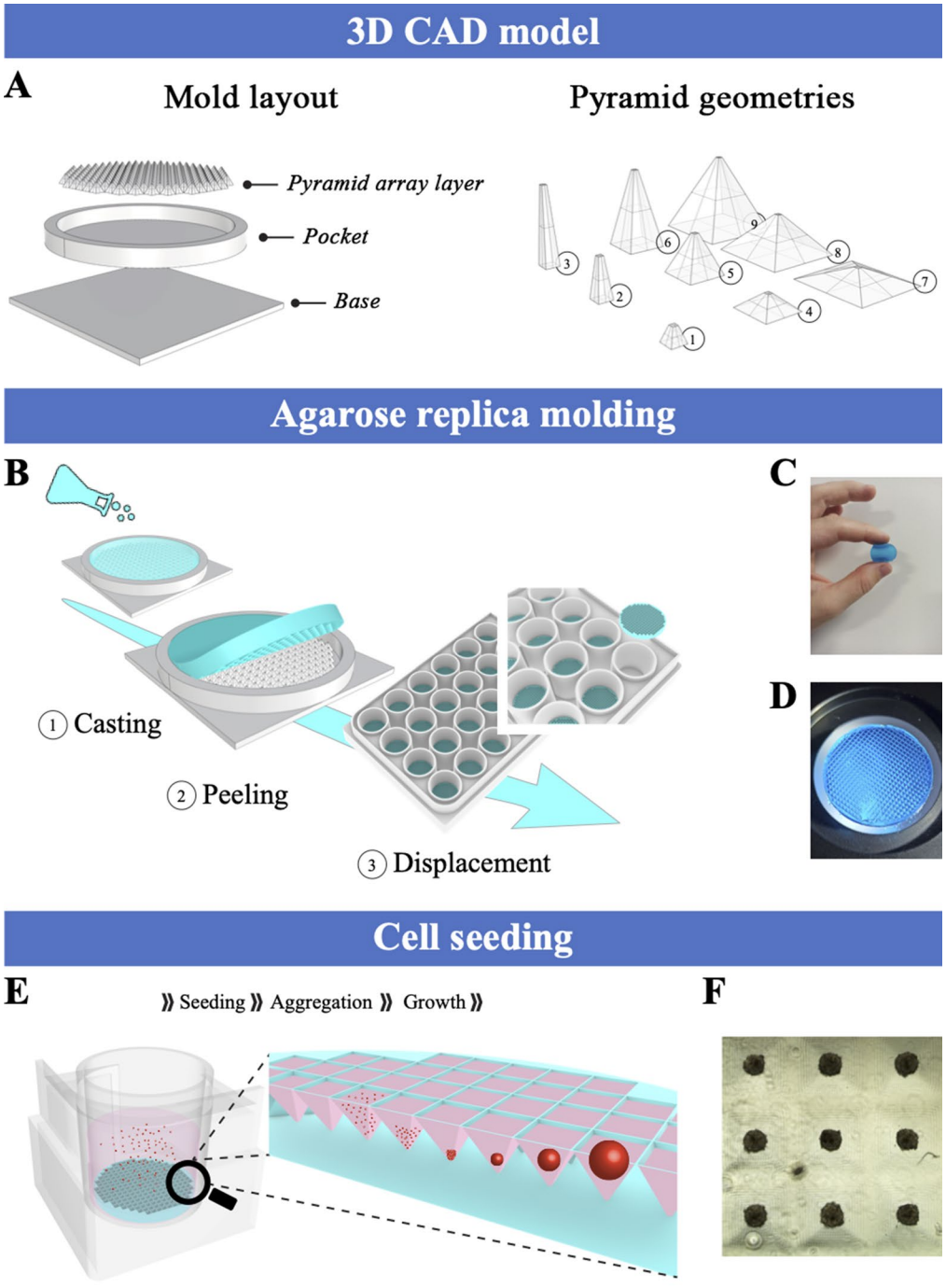

Fig. 1 Microwell inserts. **A**) Layout of the 3D printed mold (see Table 1). **B**) Schematic representation of the manufacturing process of the agarose inserts via replica molding. **C**, **D**) Agarose inserts are easily manipulated and transferred into multiwell plates. **E**) Cell seeding and scaffold-free spheroid aggregation. **F**) Brightfield micrograph of MNP spheroids cultured on 800×800 µm (width × depth) microwell insert

Scanning Electron Microscope (FE-SEM, Sigma 300VP, Zeiss Microscopy, Germany). Prior to SEM investigation, the sample was coated with a 10-nm sputtered gold layer (CCU-010 LV, Safematic GmbH, Switzerland).

Negative mold processing was used to fabricate the microwell devices using sterile ultrapure agarose hydrogel (Fig. 1B-D). Specifically, 1 g of agarose (Sigma) was dissolved in 50 mL of PBS at 90 °C and cooled to 60 °C. Then, the agarose solution was poured into the resin mold and covered with a glass slide, to avoid air bubbles on the surface and to level the solution during solidification. Detachment of the agarose replicas was performed after complete solidification with the aid of a compressed air jet. The agarose microwells were then inserted in

Table 1 Definition of the 9 microwell geometries used to generate the devices, including the number of microwell for each device

Geometry	Base (μm)	Height (μm)	Microwells per 24-well plate	Layers
1	150	150	5503	6
2	150	400	5506	16
3	150	800	5501	32
4	400	150	906	6
5	400	400	906	16
6	400	800	906	32
7	800	150	228	6
8	800	400	228	16
9	800	800	228	32

24-well plates and UV-sterilized. Microwells were stored at 4 °C in PBS supplemented with 1% penicillin/streptomycin solution.

Human iPS cell culture and differentiation in MNP spheroids

Human iPS cells (line WTSli095-A) were purchased from the European Bank for Induced Pluripotent Stem Cells (EBiSC, Oxford, UK). Human iPS cells were grown and expanded as single cells on Matrigel-coated plates at a density of 2.0×10^5 cells/cm^2 in mTeSR1 complete medium. To generate motor neuron progenitor (MNP) spheroids, the protocol disclosed by Du et al. [37] was slightly modified at the spheroid culture step (Fig. 2). Briefly, hiPSCs were dissociated by incubation in dispase solution (1 U/mL, Sigma) for 5 minutes and split (1:6) on Matrigel-coated tissue culture plates in mTeSR1 medium. On the following days, neuroepithelial progenitors (NEP) differentiation was induced by replacing the cell culture medium with neural culture medium I (NCM-I, Table S3). NCM-I was replaced every other day. On day 6, NEP cells were dissociated with dispase solution (1 U/mL) and split again 1:6 in neural culture medium II (NCM-II, Table S3). NEPs were cultured for 6 days and differentiated into OLIG2$^+$ MNPs. MNP cells were then expanded in neural culture medium III (NCM-III, Table S3). Starting from MNP cultures, cells were dissociated with dispase solution and cultured in the previously described agarose microwells in neural culture medium IV (NCM-IV, Table S3) as follows. Once dissociated, MNPs were resuspended in NCM-IV at the density of 1.8×10^5 cells/mL. 500 μL of cell suspension was added to each well of a 24-well plate hosting the microwell devices (Fig. 1E-F) and centrifuged at 300 × g for 5 minutes using a microplate swinging bucket rotor (Megafuge ST1, Thermo Scientific) to confine cells in the microwells. NCM-IV was refreshed every other day, by changing 75% of the medium, and cells were cultured as spheroids for 7 days.

Dimensional analysis and shape factors

Micrographs of the obtained MNP spheroids inside their microwells were collected on a widefield automated optical microscope (Evos M7000, Thermo Fisher Scientific). Images were collected at the final time point of differentiation (day 7). Image collection was performed in a semi-automatic way as shown in the workflow of Figure S2A, allowing to gather and analyze thousands of images. The original dataset was cleaned from micrographs containing artifacts (e.g., broadly off-target images) via image classification built in Orange 3.0 (https://orangedatamining.com) [38], according to the scheme reported in Figure S2B. To further proceed with a quantitative analysis, a DL-assisted segmentation software (Arivis Cloud, Zeiss Microscopy) was used to perform a semantic segmentation of the dataset images, using a training set of 100 manually annotated images (Figure S2C) [39]. These annotations were used to train a deep neural network which model was then used to perform a semantic segmentation of the dataset images. Starting from the area, the equivalent diameter (d) was calculated using Eq. 1 assuming the approximation of a perfectly circular sphere. Two shape factors were also calculated, the Aspect Ratio (AR), calculated using Eq. 2 and the solidity (S) calculated by Eq. 3, where d_{max} is the maximum diameter, d_{min} the minimum diameter, A the total area,

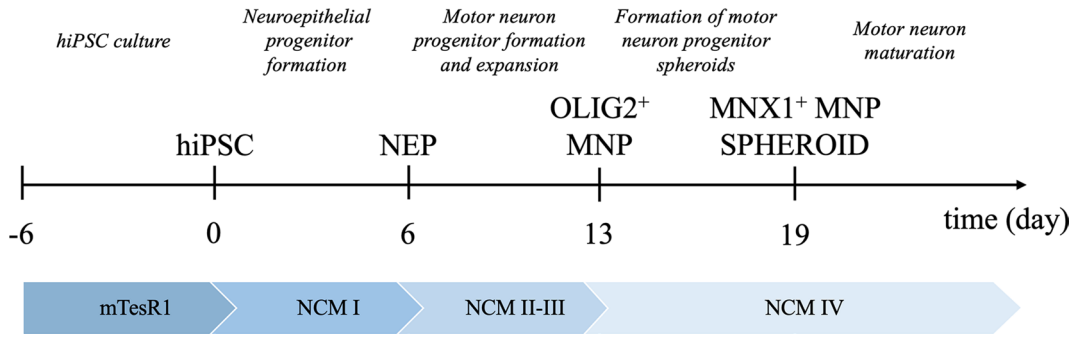

Fig. 2 Timeline and sequential steps of hiPSCs differentiation into MNP spheroids. Neuroepithelial progenitors (NEP), neural culture medium (NCM), motor neuron progenitors (MNP), and motor neurons (MN)

and A_{convex} the area of the convex hull. Only features with a solidity value $S > 0.8$ were included in the analysis, thus excluding objects with pronounced concavities/convexities, which are reliably associated to artifacts.

$$d = 2\sqrt{A/\pi} \tag{1}$$

$$AR = d_{max}/d_{min} \tag{2}$$

$$S = A/A_{convex} \tag{3}$$

Response surface method

Microwell geometries were chosen to perform a further statistical analysis, namely Response Surface Method (RSM). The entire statistical analysis was performed using the programming language R (v. 4.3.1) [40] following the statistical strategy described in previous works [41–43]. Two geometrical factors (A–the microwell side and B– the microwell depth) were considered, each having 3 levels. Then, a model was built by selecting the significantly relevant factors and tested by analysis of variance (ANOVA). The significance level was assigned as follows: $p \leq 0.1$ (.), $p \leq 0.05$ (*), $p \leq 0.01$ (**), $p \leq 0.001$ (***). The complete model is shown in Eq. 6. It should be noted that not all the terms must be present in the model. Only terms with $p \leq 0.1$ were included, while the model was considered significant with a $p \leq 0.05$. To evaluate the goodness of fit of the model, the coefficient of determination (R^2) was calculated.

$$Y = c_0 + c_1 A + c_2 B + cAB + c_4 B^2 \tag{6}$$

Immunofluorescence staining

Immunofluorescence staining was performed on cells at different stages of differentiation (hiPSCs, NEPs and MNPs) into Matrigel-coated Ibidi µ-dishes and on NMP spheroids grown in microwell devices.

At the end of each differentiation step, cells were washed with PBS and fixed with 4% PFA in PBS for 10 min at room temperature (RT). MNP spheroids (at day 7) cultured inside microwell devices were washed with PBS and incubated with 4% PFA for 10 min at RT. To facilitate spheroid harvesting and collection, agarose devices were transferred upside down in a clean 24-well plate containing 500 µL of PBS and centrifuged at 300 × g for 10 min. The agarose devices were gently removed, and spheroids were easily collected from the bottom of the well into 1.5 mL vials for further processing.

Both adherent cells and spheroids were permeabilized with permeabilization solution (0.2% TritonX-100 in PBS) for 10 min at RT, incubated with blocking solution (1% BSA in PBS) for 30 min at RT, incubated overnight at 4 °C with primary antibodies as detailed in Table S4 and revealed with secondary antibodies in blocking solution for 1 h at RT. Cytoskeletal actin and nuclei were counterstained with AlexaFluor-555 Phalloidin and DAPI, respectively. Specimens were imaged either with a Leica TCS SP8 or with a Zeiss LSM 980 laser scanning confocal microscope.

Total RNA isolation and RT-qPCR analysis

Expression levels of stemness and neuronal differentiation genes were evaluated by RT-qPCR on both adherent cells and spheroids at specific differentiation time points. Total RNA was extracted and isolated using Aurum Total RNA Mini Kit (Bio-Rad). Extracted RNA was quantified spectrophotometrically (Nanodrop, Thermo Fisher Scientific). 1 µg of total RNA was reverse-transcribed using iScript Adv cDNA Synthesis Kit for RT-qPCR (Bio-Rad) according to the manufacturer's protocol. Quantitative PCR analysis was performed on 10 ng of cDNA in a total reaction volume of 10 µL, using SsoAdvanced Universal SYBR Green Supermix (Bio-Rad) and primers (PrimePCR Assay, Bio-Rad) for the genes listed in Table S5. To identify the best housekeeping gene, an analysis of the expression level of several candidate reference genes (Table S5) was performed using geNorm v.3.5. All experiments were performed in triplicate. Gene expression levels were referred to those of control hiPSCs. The significance levels were assigned as follows: * $p < 0.05$, ** $p < 0.01$, *** $p < 0.001$, **** $p < 0.0001$. Then, a 2-way ANOVA was performed on gene expression datasets to determine to which extent the two factors (i.e., microwell width and depth) impact on gene regulation of NMP spheroids. Finally, to evaluate the dependence of gene regulation upon spheroid morphological parameters (diameter, aspect ratio and solidity), a Pearson's correlation matrix was calculated, reporting the Pearson's correlation coefficient (r) and the corresponding p-value. Two variables were considered significantly correlated if two conditions were satisfied: $|r| \geq 0.4$ and $p < 0.05$.

Results

Mold morphology

To qualify the manufacturing process, a sample for each of the nine pyramidal geometries was observed by SEM (Fig. 3). SEM micrographs clearly showed that DLP structures were characterized by a stepped geometry, which is characteristic of this layer-by-layer fabrication process. The height of these steps is fixed by the printing parameters to be 25 μm, the number of layers is reported in Table 1. In order to quantitatively assess the adherence of the printed mold to the CAD design, 30 pyramids for each experimental condition were measured by image analysis and the percentage difference with the nominal dimension was calculated. As reported in Table 2,

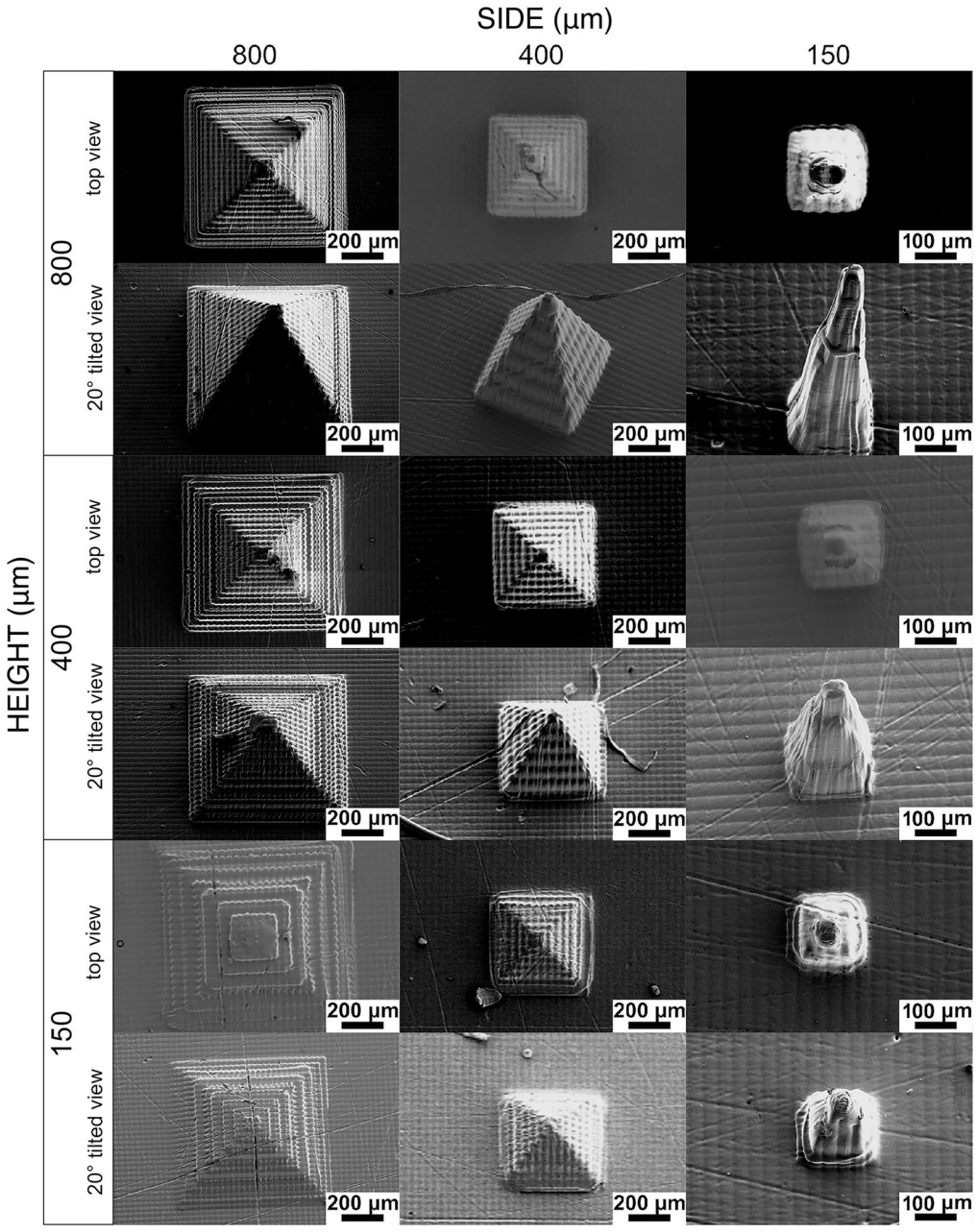

Fig. 3 SEM micrographs of the 9 pyramidal geometries obtained by DLP printing, viewed from top (0°) and under a 20° tilt angle. The stepped geometry is characteristic of DLP processing and is conditioned by the z-step of the layer-by-layer fabrication

the percentage difference between the samples and the design was always lower than 6%, which should be considered acceptable.

HiPSC differentiation into MNPs

MNP spheroids were generated starting from 2D cultures of MNPs, which were obtained following a series of developmental steps. First, hiPSCs were differentiated into NEP cells following the dual SMAD inhibition protocol for feeder-free neural induction in adherent cultures. hiPSCs exhibited typical characteristics of stem cells (i.e., large nucleus and multiple, prominent nucleoli; growth as round colonies) and they expressed typical pluripotency markers as SOX2 and NANOG (Fig. 4, top). hiPSCs were differentiated into NEP, forming a confluent cell monolayer characterized by clustering of dense opaque cellular aggregates (Fig. 4, bottom) expressing NK6 homeobox 1 (NKX6.1) (67.8 ± 5.5% positive nuclei), a transcription factor involved in ventral neural patterning and controlling the lineage specification of both neurons and glia during spinal cord development. Additionally, NEP were found to be positive for an epithelial marker, Occludin,

Table 2 Shape fidelity of 3D printed structures. Measured side (from SEM micrograph) of the pyramid structures with different nominal dimensions. The percentage difference between the measured side value and its nominal value is below 6% for all the experimental groups

Nominal side (μm)	Nominal height (μm)	Measured side (μm)		Difference (%)
		Mean	StD	
150	150	148.22	4.64	-1.19
150	400	157.11	9.52	4.74
150	800	152.60	2.96	1.73
400	150	378.63	8.54	-5.34
400	400	382.45	3.79	-4.38
400	800	403.53	17.58	0.88
800	150	793.26	31.19	-0.84
800	400	764.97	20.26	-4.37
800	800	802.13	17.42	0.27

known to be involved in the early stages of neurogenesis [44]. NEPs were differentiated in MNPs recognized by dense-core rosette structures surrounded by radially oriented single cells (Fig. 5). At this stage, immunofluorescence confirmed positivity to Oligodendrocyte Transcription Factor 2 (OLIG2), a basic Helix-Loop-Helix (bHLH) transcription factor identified as a motor neuron progenitor marker (72.4 ± 5.9% positive nuclei) [45], indicating the successful ventralization of NEP into MNPs. MNP were also moderately positive to Neuronal Differentiation 1 (NEUROD1, 32.8 ± 13.3% positive nuclei) and Neurogenin 2 (NEUROG2, 19.5 ± 2.9% positive nuclei), two bHLH transcription factors important during neurogenesis and governing the transition of neural progenitor cells to neurons.

Differentiation was also confirmed at the mRNA level using RT-qPCR for neuronal markers specific to the NEP and MNP stages (Fig. 6A-B). Specifically, *NKX6.1* levels were significantly upregulated during differentiation of hiPSCs into NEPs, and the transcription factors *OLIG2*, *NEUROD1* and *NEUROG2* were significantly upregulated following differentiation into MNPs.

Segmentation results

One representative micrograph for each microwell geometry is reported in Fig. 7A as an example of the spheroid segmentation procedure. Spheroids were correctly segmented, as it can be observed by the color mask indicating the individuated features superimposed to the brightfield microscopies. From a visual inspection, spheroid dimensions increased with increasing the base side, while the height of the pyramids had a smaller influence. We could observe that control cells cultivated in a Petri dish resulted in non-uniform spheroids of different shapes and sizes (Fig. 7B). The box plot in Fig. 7C confirmed this initial analysis for the diameter. Microwells

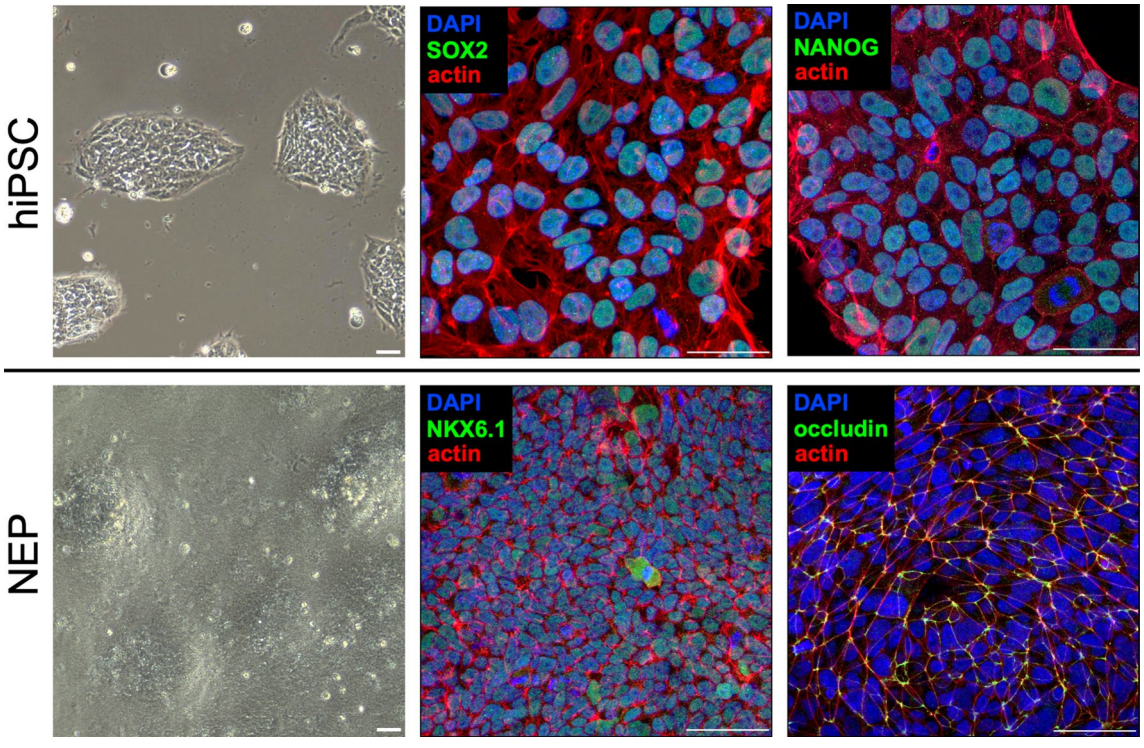

Fig. 4 hiPSC differentiation into NEP. Top) Phase contrast micrographs of hiPSC colonies and immunofluorescence micrographs for iPS markers SOX2 and NANOG. Scale bar = 50 μm. Bottom) Phase contrast micrographs of NEP confluent layer and immunofluorescence micrographs for NEP markers NKX6.1 and Occludin. Scale bar = 50 μm

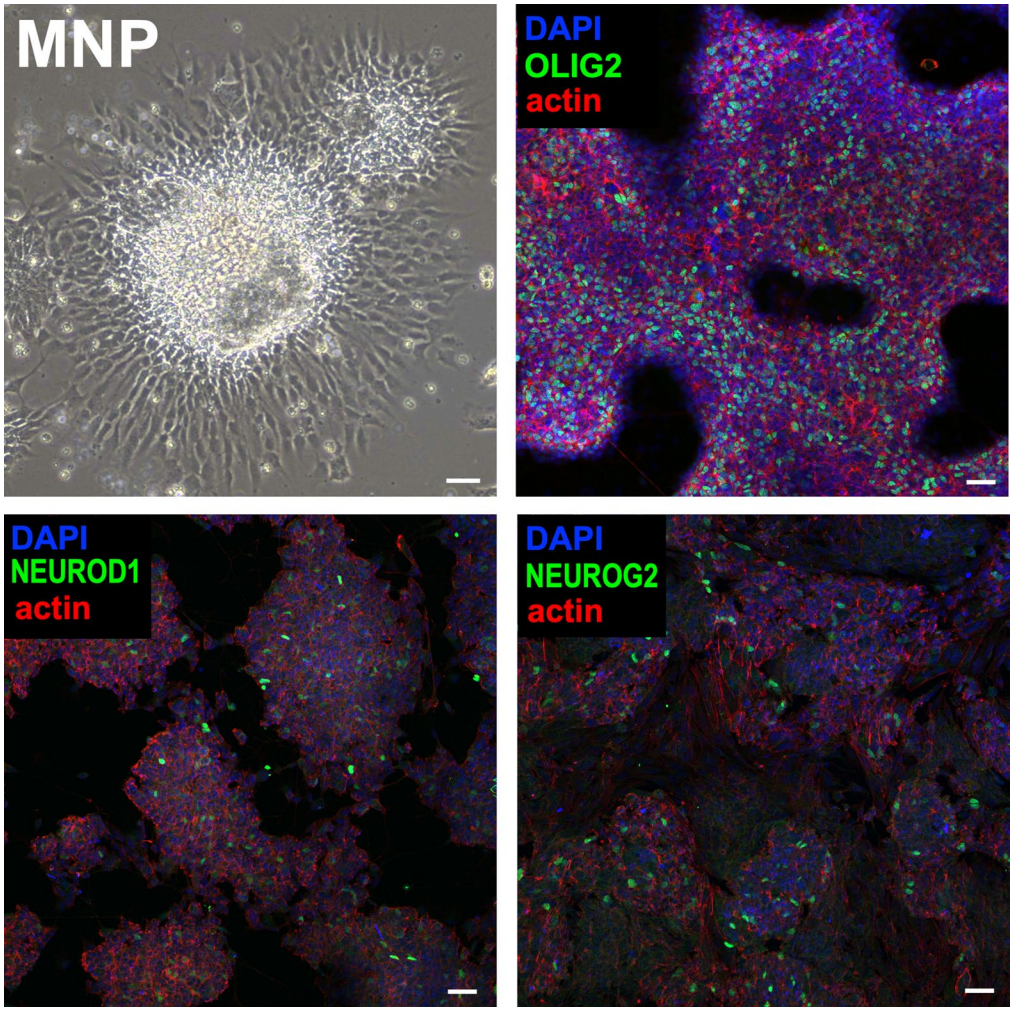

Fig. 5 Differentiation into MNP. Phase contrast and immunofluorescence micrographs of MNP rosettes stained for OLIG2, NEUROD1 and NEUROG2 markers. Scale bar = 50 µm

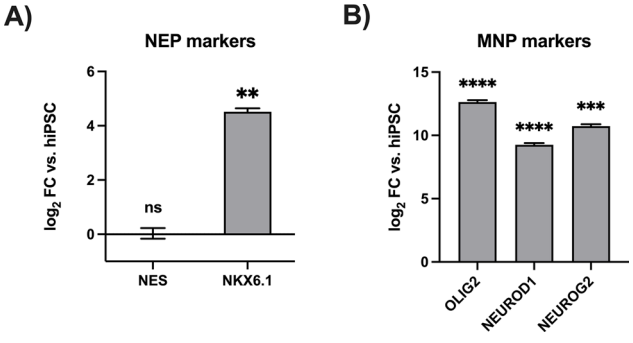

Fig. 6 Expression levels of differentiative markers. Analysis of the mRNA levels for NEP markers (NES and *NKX6.1*) (**A**) and MNP markers (*OLIG2*, *NEUROD1*, and *NEUROG2*) (**B**) normalized to the levels of hiPSC controls. Results were analyzed by ANOVA followed by post hoc testing. The significance levels were assigned as follows: ** $p < 0.01$, *** $p < 0.001$, **** $p < 0.0001$

with a depth of 150 µm did not give uniform spheroids, which also tended to detach from their pocket (Figure S3). For this reason, only microwells with a depth of 400 and 800 µm were included in the following analyses. Spheroids had a mean diameter in the 38–160 µm range, which was shown to increase with increasing the microwell side. In the case of cells cultivated on low-adherence Petri dishes, the mean value resulted to be almost 45 µm with a wide distribution, which resulted in a maximum diameter of almost 260 µm. Interestingly, the size distributions obtained by the microwell devices (grey and red boxes) resulted to be Gaussian-like, while in the case of the Petri dishes (blue boxes), the distributions resulted to be skewed towards the lower values and heavy-tailed indicating the presence of large aggregates of cells. This result was also confirmed numerically by the values of skewness (that indicates how distant is the distribution from normality that has a skewness of 0) and kurtosis (that indicates how "thick" the distribution tail

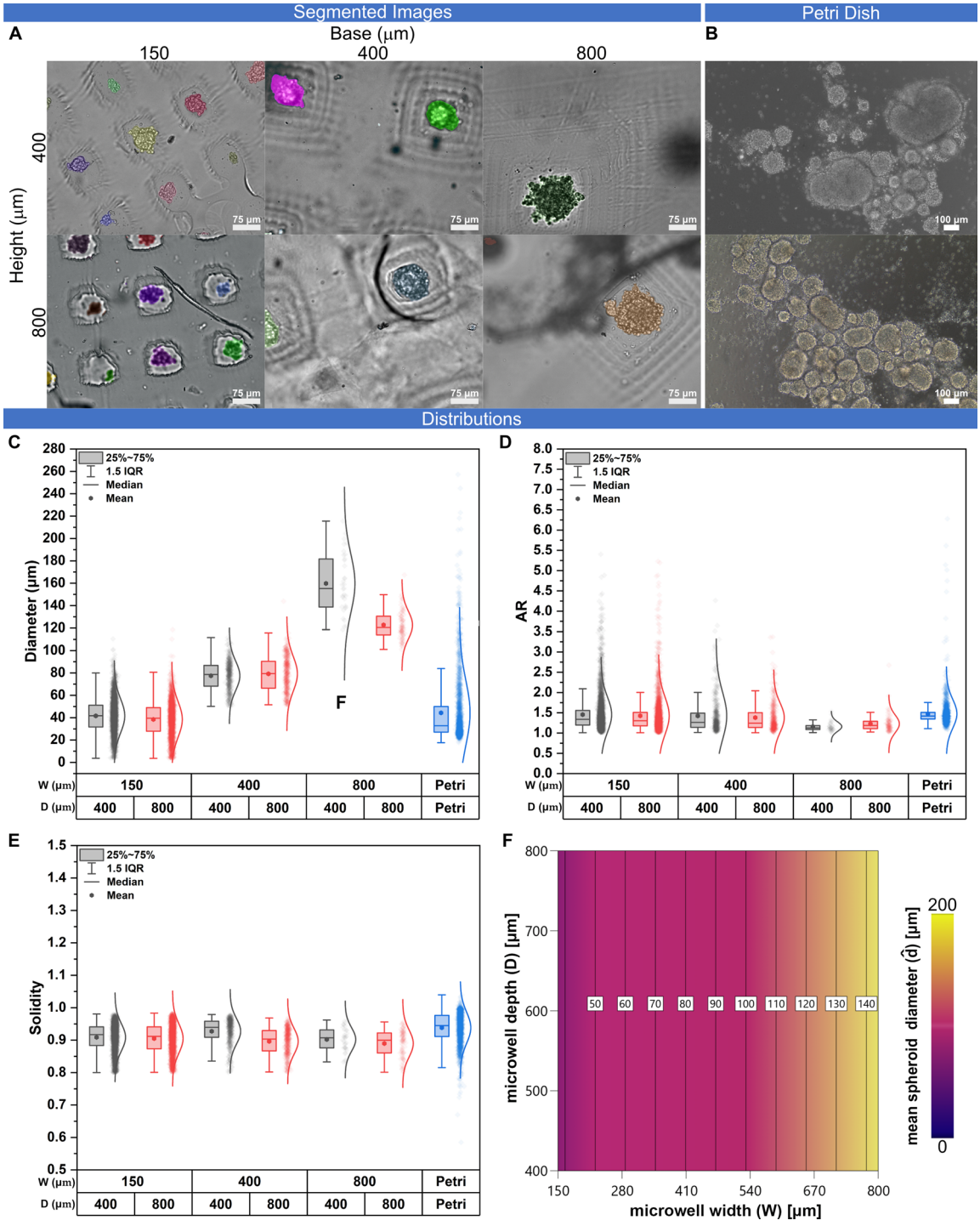

Fig. 7 Dimensional and shape analysis from brightfield image segmentation of MNP spheroids. **A**) Segmented micrographs of spheroids formed into the microwell arrays. **B**) Brightfield micrographs of spheroids formed on a Petri dish. **C**-**E**) Box plot of the distribution of mean diameter, aspect ratio (AR) and solidity for the different experimental groups as extracted from segmented images. An AR value close to 1 indicates a shape close to a sphere. A solidity value close to 0 indicates the presence of pronounced convexities or concavities. **F**) The contour plot of the RSM model for mean diameter reveals that the spheroid diameter is dictated by the microwell width

compared to the normal distribution, the kurtosis for a normal distribution is 0) reported in Table 3. Both values resulted in the highest among the ones calculated for the area and diameter distributions. Two additional shape factors were examined: the spheroid aspect ratio (AR, Fig. 7D), which is the ratio among the major and minor axes and has a minimum value of 1, and the solidity (Fig. 7E), which is the ratio among the total area and the total area of the convex hulls (if present) with a maximum value of 1 indicating a solid object. The mean value of AR was always slightly higher than 1, and to some extent decreased with increasing the microwell side, resulting in a minimum value of about 1.20 in the case of the largest wells (800 μm). The highest value was obtained for spheroids grown on low-adherence Petri dishes, which gave an AR of almost 1.48. The mean values of the solidity for the different distributions were all above 0.9 with the highest value obtained by the cells cultivated on Petri dishes (~0.95).

The RMS models of the mean diameter (Fig. 7F) confirmed the non-statistical relevance of the microwell depth on the resulting spheroid diameter. The equation for the mean spheroid diameter ($\widehat{d}$) is reported below:

$$\widehat{d} = 1.32 \bullet 10^{1} + 0.16 * W \quad (7)$$

indicating a linear dependence of the spheroid diameter on the sole microwell width (further details in Tables S6-S8).

MNP spheroids characterization

MNP cells, obtained and characterized as previously described, were dissociated and cultured on six distinct agarose microwells geometries in neural culture medium IV (NCM-IV, Table S3). MNP spheroids were allowed to grow and differentiate in the agarose microwells for 7 days and subsequently analyzed for the positivity to motor neuron differentiation markers. Immunofluorescence showed the marked expression of ISL1 and MNX1

Table 3 Descriptive statistics of the dimensional parameters studied in the segmentation process (Diameter, aspect ratio, Solidity) of the MNP spheroids. For each parameter, the mean, the standard deviation (StD), the skewness (Skew), the kurtosis (Kurt), the minimum value (Min), the first quartile (Q1), the median, the third quartile (Q3), the maximum value (Max), and the interquartile range (IQR = Q3-Q1) associated to each microwell geometry (depth, D and width, W) have been reported

SPHEROID DIAMETER (d)											
W (μm)	**D (μm)**	**Mean (μm)**	**StD (μm)**	**Skew**	**Kurt**	**Min (μm)**	**Q1 (μm)**	**Median (μm)**	**Q3 (μm)**	**Max (μm)**	**IQR (μm)**
150	400	41.61	15.16	0.16	0.24	3.68	31.69	41.80	51.10	110.44	19.41
	800	38.44	15.72	0.00	0.14	3.62	27.88	39.53	48.97	118.57	21.09
400	400	77.44	13.10	-0.10	-0.50	50.12	68.18	78.60	86.71	111.64	18.53
	800	79.21	15.56	0.15	-0.37	51.58	66.39	79.39	90.37	143.87	23.98
800	400	159.81	26.46	0.34	-0.84	118.60	138.67	155.28	181.66	215.61	42.99
	800	122.66	12.44	0.80	0.84	101.01	114.00	120.48	130.46	167.38	16.47
Petri		44.30	28.89	2.58	8.67	17.61	27.06	32.81	50.00	257.29	22.95
SPHEROID ASPECT RATIO (AR)											
W (μm)	**D (μm)**	**Mean**	**StD**	**Skew**	**Kurt**	**Min**	**Q1**	**Median**	**Q3**	**Max**	**IQR**
150	400	1.45	0.43	3.25	17.85	1.01	1.20	1.34	1.56	6.75	0.36
	800	1.43	0.46	5.11	53.03	1.01	1.18	1.30	1.51	9.57	0.33
400	400	1.42	0.58	7.03	82.53	1.01	1.14	1.26	1.49	9.38	0.35
	800	1.38	0.36	2.15	6.04	1.01	1.14	1.24	1.50	3.37	0.36
800	400	1.16	0.12	1.66	2.99	1.01	1.09	1.12	1.18	1.53	0.10
	800	1.23	0.22	3.85	21.95	1.02	1.11	1.19	1.29	2.67	0.18
Petri		1.48	0.36	10.00	155.87	1.08	1.35	1.42	1.51	8.97	0.16
SPHEROID SOLIDITY (S)											
W (μm)	**D (μm)**	**Mean**	**StD**	**Skew**	**Kurt**	**Min**	**Q1**	**Median**	**Q3**	**Max**	**IQR**
150	400	0.91	0.04	-0.71	-0.26	0.80	0.88	0.92	0.94	0.98	0.06
	800	0.91	0.05	-0.43	-0.72	0.80	0.87	0.91	0.94	0.98	0.07
400	400	0.93	0.04	-1.19	0.96	0.80	0.91	0.94	0.96	0.98	0.05
	800	0.90	0.04	-0.52	-0.59	0.80	0.87	0.90	0.93	0.97	0.06
800	400	0.90	0.04	-0.17	-0.79	0.83	0.88	0.91	0.93	0.96	0.06
	800	0.89	0.04	-0.49	-0.84	0.80	0.86	0.90	0.92	0.96	0.06
Petri		0.94	0.05	-1.11	2.69	0.58	0.91	0.94	0.98	1.04	0.06

(which are both required for the maturation of functional pluripotent stem cell-derived MNs [45, 46]) in all the experimental groups (Fig. 8). Additionally, MNP spheroids were assayed for SOX2 (a neural progenitor marker [47]) and for proliferation marker protein Ki-67 (Fig. 9). These results were also quantified at the mRNA level by RT-qPCR analysis (Fig. 10). All groups showed increased mRNA levels of *ISL1* and *MNX1* compared to hiPSCs. A two-way ANOVA test was used to further elucidate the effects of the two factors (microwell width and depth) on the resulting gene regulation. *ISL1* mRNA levels show a consistent and extremely significant interaction (24.8% of total variance, $p < 0.0001$), thus implying that the effects of each factor differ as a function of the level of the other factor. The (positive) main effect of microwell width (70.1% of the total variance, $p < 0.0001$) was much stronger than that of depth (3.74% of the total variance, $p < 0.0001$). Concerning *MNX1*, we report a moderate but highly significant "cross-over" interaction (10.9% of total variance, $p = 0.0099$) with a positive main effect of microwell width (79% of total variance, $p < 0.0001$), while the effect of depth (0.73% of total variance, $p = 0.35$) was not significant. *SOX2* showed a general upregulation trend for all the spheroid conditions compared to hiPSCs, in line with recent evidence suggesting that the gene is involved not only in the maintenance of pluripotency, but also in the differentiation and development of motor neurons [48]. Following two-way ANOVA, we report a strong and highly significant cross-over interaction (37.5% of the total variance, $p < 0.0001$), which hampers the interpretation of main effects. As a general consideration, we can observe a strongly enhanced expression for the largest microwell geometry (width 800 µm, depth 800 µm).

Concerning *MKI67*, we report a strong and extremely significant cross-over interaction (45.56% of the total variance, $p < 0.0001$).

To understand if the regulation of gene expression was dependent on the spheroid physical parameters (size, aspect ratio and solidity), we computed the correlation matrix (Fig. 11A) and the corresponding p-values (Fig. 11B). Pearson's correlation coefficient indicates if a linear correlation exists between the two variables, considering values of +1 or -1 as representative of a perfect linear correlation (direct and inverse, respectively) and values between −0.4 and 0.4 as not correlated.

The expression of differentiation markers *ISL1* and *MNX1* was found to be inversely correlated to the aspect

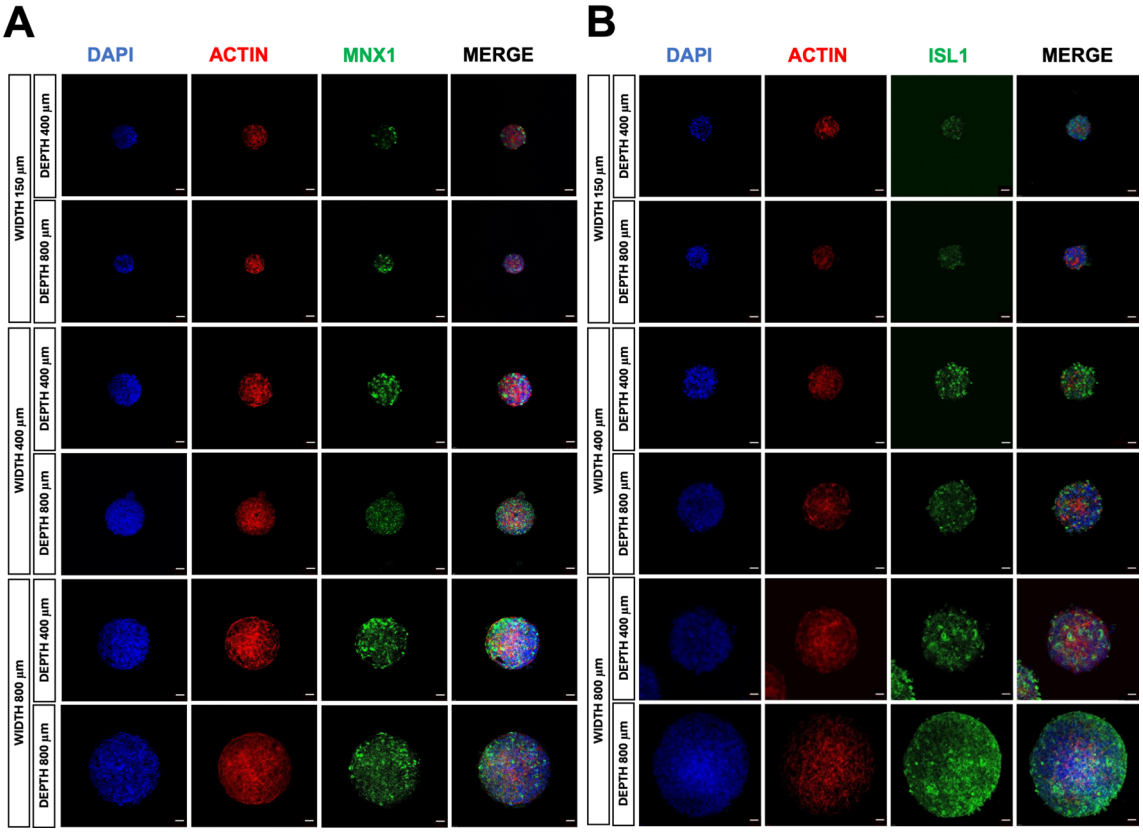

Fig. 8 Immunostaining for ISL1 and MNX. Confocal micrographs of whole-mount immunostaining for MNX1 (**A**) and ISL1 (**B**) on MNP spheroids after 7 days of culture in agarose microwells of different sizes. Cytoskeletal actin and nuclei are counterstained with AlexaFluor 555 phalloidin (red) and DAPI (blue), respectively. Scale bar = 50 µm

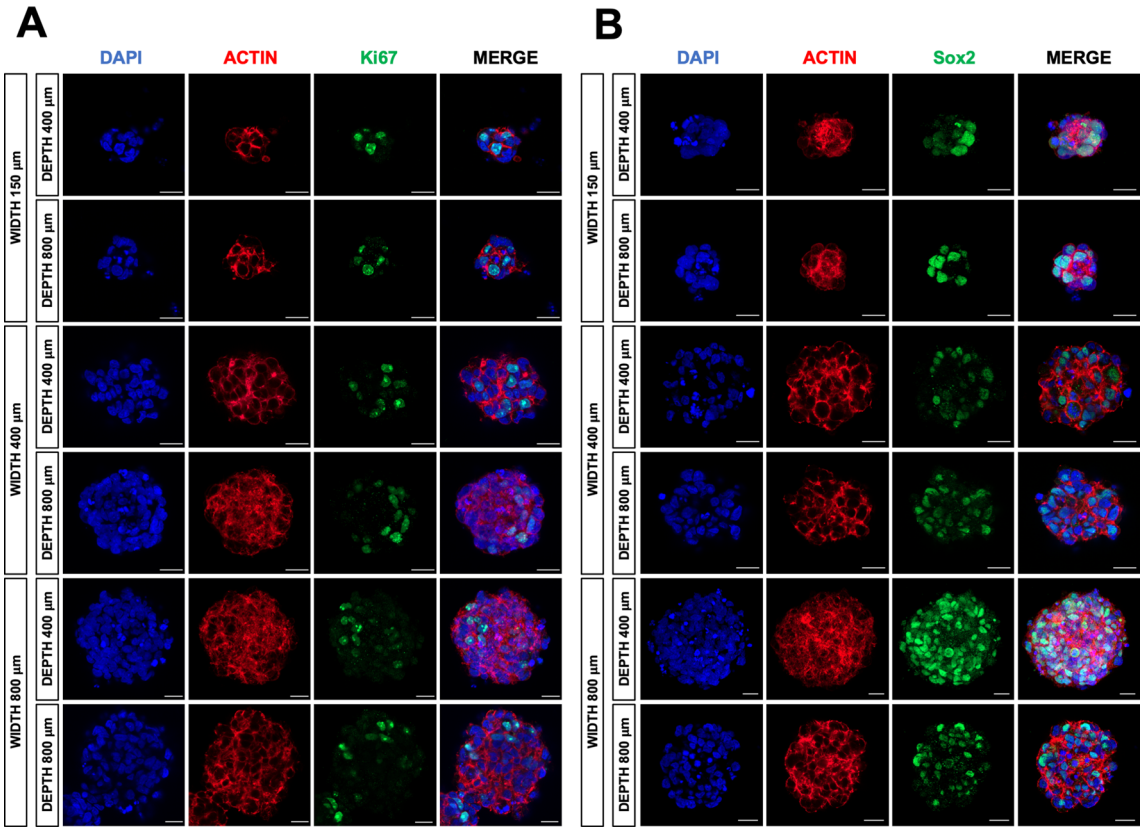

Fig. 9 Immunostaining for SOX2 and MKI67. Confocal micrographs of whole-mount immunostainings for MKI67 (**A**) and SOX2 (**B**) on MNP spheroids after 7 days of culture in agarose microwells of different sizes. Cytoskeletal actin and nuclei are counterstained with AlexaFluor 555 phalloidin (red) and DAPI (blue), respectively. Scale bar = 50 µm

ratio ($r = -0.87$, $p = 0.02$; $r = -0.9$, $p = 0.01$). A similar trend was observed also for *SOX2* and *MKI67*, but correlation failed to reach significance ($r = -0.9$, $p = 0.05$; $r = -0.63$, $p = 0.19$).

MNX1 mRNA levels also showed a direct correlation with the spheroid diameter ($r = 0.83$, $p = 0.03$) which, in turn, was shown to be linearly dependent from the microwell width according to the RSM model.

Discussion

During the past decade, several 3D neuronal platforms have been proposed to model the human brain in vitro, with the aim to fill the gap between preclinical and clinical research [23, 49]. Among these, human spheroids have emerged for their simplicity and scalability, making them a preferred choice for high-throughput drug screening assays. Many research efforts have been spent to identify the most suitable techniques to drive spheroids formation, growth and maturation. The current study offers a preliminary analysis focused on assessing the impact of geometric confinement on motor neuron spheroid differentiation.

We adopted a negative mold technique to fabricate microwell arrays according to a parametric design for culturing of hiPSC-derived MNP spheroids with high scalability and reproducibility at different levels of geometrical confinement. Square pyramid microwells were chosen among the geometries reported in the literature [50, 51] for their unitary packing factor to facilitate cell deposition and organization during sphere formation. Our system allowed culturing a large number of spheroids in a reliable and reproducible way, which is very attractive in experimental settings where high throughput applications are required. The thin layer of agarose arrays has been designed to fit the bottom of cell culture plates, enabling seeded cells to be partitioned into the microwells by mild centrifuging. The multiwell array configuration also allowed single-step media change without the risk of aspirating the samples, which is one of the main spheroids culturing-related issues.

The use of microwell arrays has been previously described in the literature [52, 53]. However, many fabrication approaches require expensive equipment, laborious manufacturing strategies, and specialized expertise. The use of DLP 3D printing overcomes these limitations. Simplicity and affordable costs have made DLP more accessible and very popular even among the general audience. In response to the increase in demand and

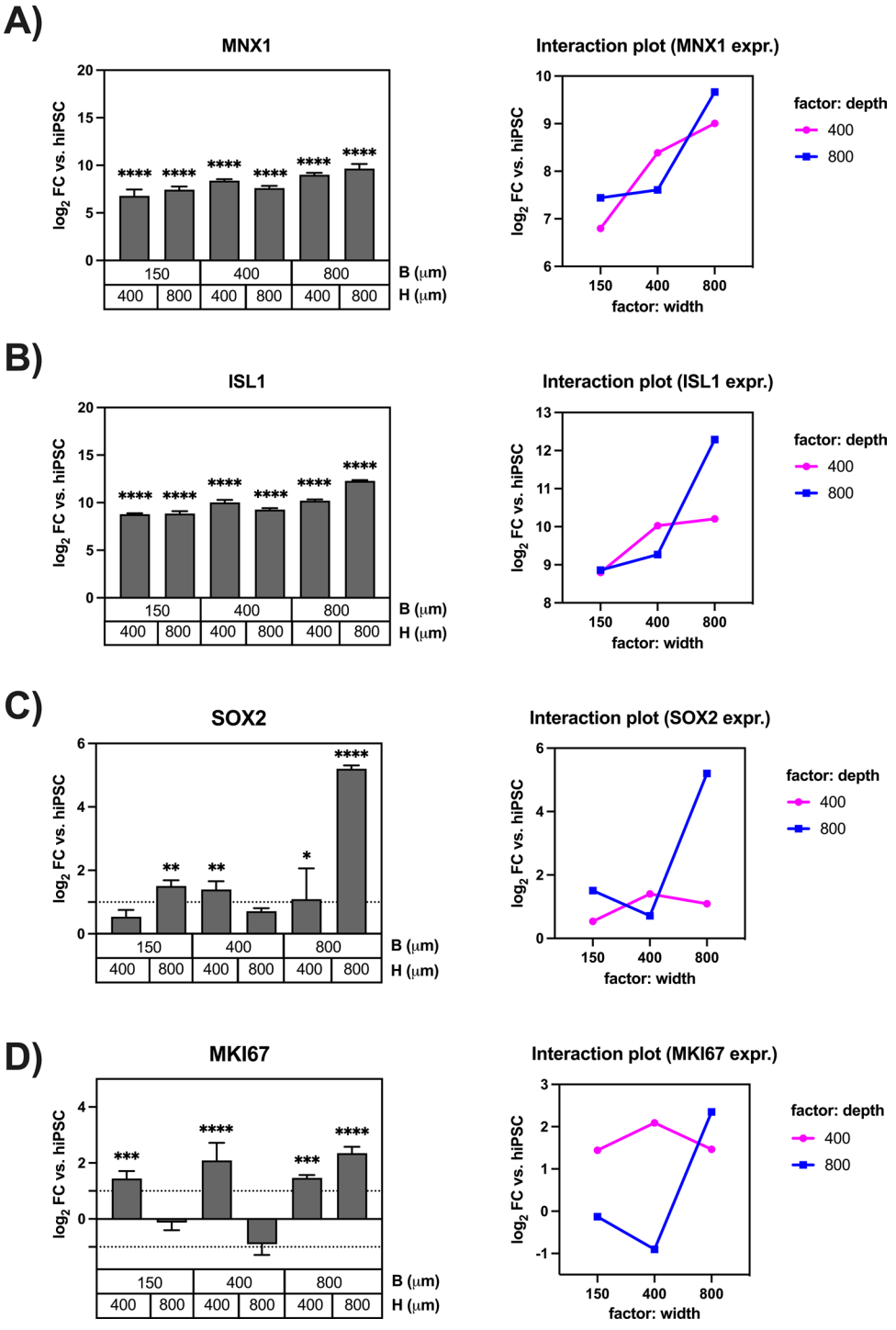

Fig. 10 Analysis of gene expression on MNP spheroids. Bar charts of the mRNA levels for *MNX1* (**A**), *ISL1* (**B**), *SOX2* (**C**) and *MKI67* (**D**) genes normalized to hiPSC controls. Significance levels were assigned as follows: * $p < 0.05$, ** $p < 0.01$, *** $p < 0.001$, **** $p < 0.0001$. In (**C**, **D**) a two-fold change threshold is represented with a dotted line. For each gene, an interaction plot is reported to visually determine the relative impact of the two factors (microwell width and depth) on the gene expression levels

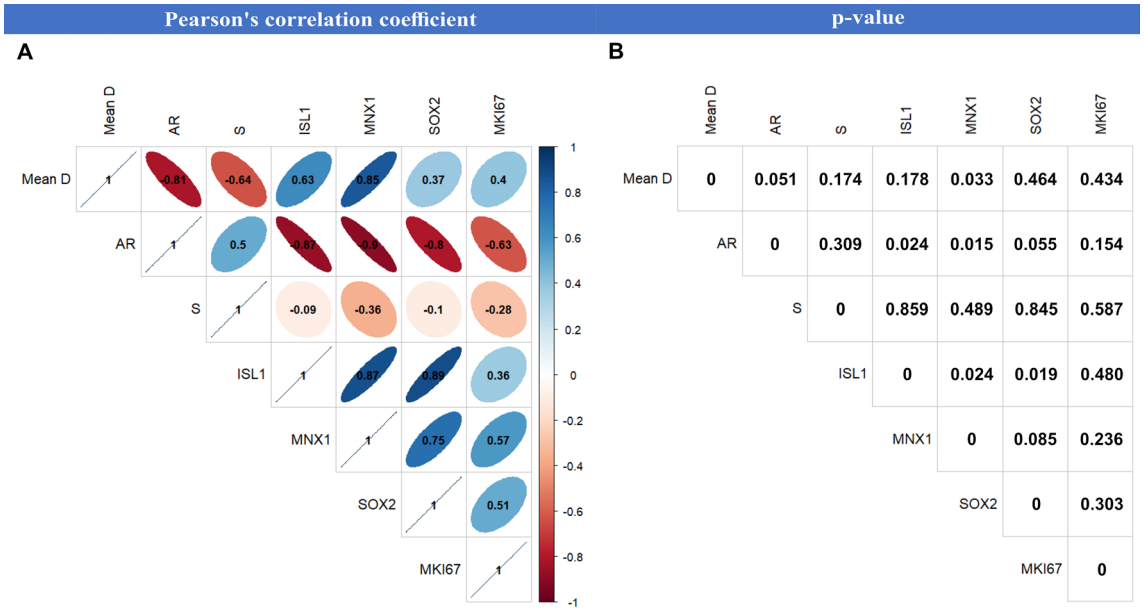

Fig. 11 Correlation matrix. **A**, **B**) Correlation matrix calculated using Pearson's method (**A**) and corresponding significance levels (**B**) of dimensional/shape descriptors and mRNA levels for MNP spheroids cultured on microwell arrays. Variables with $|r| \geq 0.4$ and a p-value < 0.05 should be considered as significantly correlated

popularity, high-resolution low-cost 3D printers are now available, while rapid technological advances promise a further performance increase in the near future [54, 55].

Several microwell systems for spheroid generation have also been proposed [50, 56], some of them even integrating functional read-outs or monitoring systems (e.g., MEA electrodes). However, these systems are typically restricted to the manufacturer's design, both for the microwell geometry and for the materials adopted. Since it is known that both substrate chemical composition [57] and microwell geometry [58] may play a role in determining cell fate, in the present work we chose to parametrically explore a set of microwell geometries for their effect on the differentiation of MNP spheroids. Specifically, by replicating DLP-produced master molds with a hydrogel material, we were able to produce arrays of pyramidal microwells with distinct geometries characterized by different width and depth levels. We used agarose as an economic and efficient solution to provide cells with a non-adhesive substrate, which would indeed drive the formation of spheroids. We then took advantage of automated microscopy and AI-based segmentation and analysis to characterize spheroids in terms of distribution of relevant morphological parameters (i.e., equivalent diameter, aspect ratio and solidity). For the equivalent diameter, in particular, a RSM model has been used to express it as a function of microwell geometrical features (i.e., microwell width and depth). The mean spheroid diameter was found to be a linear function of the microwell width, while the contribution of depth was not significant. This can be readily explained in terms of cell partitioning at the seeding stage, as larger microwells are expected to gather a larger number of cells.

Analyzing the mRNA levels of genes of interest for MNP spheroid maturation, we found a significant interaction of the two factors (microwell width and depth), indicating that the outcome of each factor was conditioned by the level of the other factor. A strong interaction may indeed hamper the explanation of the main effects. However, as a general trend, the main effect of the microwell width was larger (accounted for a larger percentage of the total variance) than that of the microwell depth.

MNX1 is a specific spinal motor neuron marker and its inactivation in developing MNs can induce a switch toward interneuron fate [59]. *ISL1* is a member of the LIM/homeodomain family of transcription factors, it is expressed in all MN subtypes, and it has been demonstrated to promote MN differentiation and suppress the interneuron fate [46, 60]. Lee and colleagues [61] showed that the use of larger microwell arrays (≥ 150 μm) promotes the differentiation of a higher number of ISL1/2-positive MNs on neurospheres cultured in a 3D GelMA hydrogel. Our results confirm these findings and corroborate the impact of microwell customization on hiPSCs-derived MN differentiation by increasing *ISL1* and *MNX1* mRNA expression in MNP spheroids. Likewise, a general upregulation trend vs. hiPSCs could be observed for *SOX2*, which plays a crucial role in the cell differentiation of the central nervous system. Conversely, *MKI67*, related to cell proliferative capacity, showed contrasting results for the different microwell geometries.

The potential relationship between gene regulation and spheroid morphological parameters was analyzed by the calculation of a Pearson's coefficient matrix. Although this represents a simplified approach, which neglects potential higher order effects, it still gives an overall outlook on correlation trends. The spheroid AR was found as the most relevant morphological descriptor correlated to the expression of transcriptional factors related to the MN development.

Our data shows the possibility to scale-up the culture of size-controlled spheroids up to 160 μm in diameter, which can be considered a reasonable upper threshold to avoid the occurrence of a necrotic core with prolonged culturing time [62]. As already reported by Hwang et al. [31], lineage differentiation of embryonic stem cells could be influenced by the size of the embryo bodies, thanks to the differential gene expression of the WNT pathway. Furthermore, differentiation capacity of hiPSCs is also affected by the initial cell number seeding [63], i.e., iPSC spheroids with a higher cell number show a lower differentiation capability, presumably due to the insufficient supply of growth factors [64].

While our study successfully demonstrates the impact of microwell geometry on spheroid development, this extends to the precursor stage only, restricting further applications in studies requiring mature MNs, such as neurodegenerative disease models. Although our work does not address final MN maturation, this step has been extensively described in the literature [37, 45], where dissociating MNP spheroids into single cells and further culturing them with Compound E results in functionally mature MNs. While our study is not designed to fully elucidate the molecular mechanisms linking geometrical confinement to spheroid development, it highlights the association between microwell shape and *MNX1*/*ISL1* mRNA expression—key regulators of MN maturation. Further investigation will be needed to uncover novel mechanobiological pathways involved in cell fate determination. Additionally, while our approach focuses solely on neuronal progenitor cells, co-culturing with other cell types, such as glial or muscle cells, could enhance the physiological relevance of the model. Regarding DLP 3D printing, a key limitation is the stair-stepping artefacts on printed surfaces, which may affect cell attachment and organization. Future studies could explore alternative fabrication techniques, such as two-photon polymerization or hybrid manufacturing approaches, to improve surface smoothness and reproducibility, widening the range of printable materials. Overall, our approach allows the customization of microwell devices for the scalability of size-controlled motor neuron spheroid addressing culture issues affecting conventional cell culture approaches and underscores the effect of geometry and shape on regulating motor neuron differentiation.

Conclusion

Given the importance of spatial confinement in driving the neuronal fate acquisition of pluripotent stem cells, in this work we investigated the influence of microwell dimensions on spheroid growth and maturation. We exploited DLP 3D printing for the replica molding of agarose pyramidal microwells with distinct parametrized geometries, which were used for the culture of hiPSC-derived motor neuron progenitors into spheroids. Our results indicate that the microwell geometry significantly influences the spheroid size and other morphological descriptors (aspect ratio and solidity), as well as the expression of early motor neuron markers such as *MNX1* and *ISL1*, which are essential for the maturation of functional MNs.

Overall, our results shed new light on the geometrical regulation of stem cell fate and the proposed platform may result in an easily scalable tool for basic research applications in the field of precision medicine.

Declarations

Supplementary Information

The online version contains supplementary material available at https://doi.org/10.1186/s13287-025-04547-4.

Supplementary Material 1

Acknowledgements

The authors declare that they have not use AI-generated work in this manuscript.

Author contributions

Eleonora Mello: Methodology, Investigation, Writing-Original Draft. Stefano Sorrentino: Conceptualization, Methodology, Writing-Original Draft. Alessio Bucciarelli: Methodology, Formal Analysis, Data Curation, Visualization, Writing-Original Draft. Ermanno Cordelli: Formal Analysis, Data Curation, Visualization, Writing-Review & Editing. Elisa De Luca: Investigation. Haakon Nygaard: Writing-Review & Editing. Stefan Wendt: Writing-Review & Editing. Alberto Rainer: Resources, Validation, Formal Analysis, Supervision, Writing-Review & Editing. Lorenzo Moroni: Writing-Review & Editing, Funding Acquisition, Project Administration, Supervision. Giuseppe Gigli: Funding Acquisition, Project Administration. Alessandro Polini: Writing-Review & Editing, Conceptualization, Supervision. Pamela Mozetic: Conceptualization, Methodology, Formal Analysis, Writing-Original Draft, Writing-Review & Editing, Supervision.

Funding

AR acknowledges project CAL.HUB.RIA (Italian Ministry of Health, Operational Health Plan, Trajectory 4, ID T4-AN-09). PM, EDL and AP acknowledge the "National Center for Gene Therapy and Drug based on RNA Technology" (CN00000041 CN3 RNA), funded by the European Union - Next Generation EU-NRRP M4.C2- Investment 1.4. EC acknowledges "Polo High Tech Lecce", funded by the Italian Ministry of Health, Health Operational Plan - Development and Cohesion Fund 2014–2020, Trajectory 4 (grant nr. T4-AN-01, OS2, CUP: F83C22001560003). The authors are grateful to the "Tecnopolo per la medicina di precisione" (TecnoMed Puglia) - Regione Puglia: DGR n.2117 del 21/11/2018, CUP: B84I18000540002. This work was supported by the Italian Ministry of Research, under the complementary actions to the NRRP "Fit4MedRob - Fit for Medical Robotics" Grant (# PNC0000007).

Data availability

Data will be made available on reasonable request.

Declarations

Ethics approval and consent to participate

The WTSIi095-A iPS cell line, available at EBiSC, has been generated by the Wellcome Sanger Institute under the framework of the project "Human Induced Pluripotent Stem Cell Initiative - HIPSCI" funded by the Wellcome Trust and Medical Research Council and approved by the NRES Committee Yorkshire and the Humber– Leeds West (approval 15/YH/0391 dated 11 Aug 2015). The present research has received positive review by the local ethical committee (CNR Research Ethics and Integrity Committee, approval #0323823 17/09/2024).

Consent for publication

Not applicable.

Competing interests

The authors declare there is no competing interest.

Author details

[1]Institute of Nanotechnology (NANOTEC), National Research Council, c/o Campus EcoTekne, via Monteroni, 73100 Lecce, Italy
[2]Department of Mathematics and Physics "Ennio De Giorgi", University of Salento, via Arnesano, 73100 Lecce, Italy
[3]Division of Neurology, Djavad Mowafaghian Centre for Brain Health, University of British Columbia, Vancouver V6T 1Z3, Canada
[4]BIOtech Research Center, European Institute of Excellence on Tissue Engineering and Regenerative Medicine, University of Trento, Via Delle Regole 101, 38123 Trento, Italy
[5]Department of Experimental Medicine, University of Salento, via Monteroni, 73100 Lecce, Italy
[6]Center for Biomolecular Nanotechnologies, Italian Institute of Technology, Via Barsanti, 73010 Arnesano, Lecce, Italy
[7]Department of Psychiatry, Djavad Mowafaghian Centre for Brain Health, University of British Columbia, Vancouver V6T 1Z3, Canada
[8]Department of Engineering, Università Campus Bio-Medico di Roma, Via Álvaro del Portillo 21, 00128 Rome, Italy
[9]Fondazione Policlinico Universitario Campus Bio-Medico, via Álvaro del Portillo 200, 00128 Rome, Italy
[10]Department of Complex Tissue Regeneration, MERLN Institute for Technology- Inspired Regenerative Medicine, Maastricht University, Universiteitsingel 40, Maastricht 6229ER, The Netherlands

Received: 1 August 2024 / Accepted: 18 July 2025
Published online: 31 July 2025

References

1. Hopkins AM, DeSimone E, Chwalek K, Kaplan DL. 3D in vitro modeling of the central nervous system. Prog Neurobiol. 2015;125:1–25. https://doi.org/10.1016/J.PNEUROBIO.2014.11.003.
2. Gibbons HM, Dragunow M. Adult human brain cell culture for neuroscience research. Int J Biochem Cell Biol. 2010;42:844–56. https://doi.org/10.1016/J.BIOCEL.2009.12.002.
3. Struzyna LA, Watt ML. The emerging role of neuronal organoid models in drug discovery: potential applications and hurdles to implementation. Mol Pharmacol. 2021;99:256–65. https://doi.org/10.1124/MOLPHARM.120.000142.
4. Osaki T, Sivathanu V, Kamm RD. Engineered 3D vascular and neuronal networks in a microfluidic platform. Sci Rep 2018. 2018;8:1. https://doi.org/10.1038/s41598-018-23512-1.
5. Sharma R, Smits IPM, De La Vega L, Lee C. Willerth, 3D Bioprinting pluripotent stem cell derived neural tissues using a novel fibrin Bioink containing drug releasing microspheres. Front Bioeng Biotechnol. 2020;8. https://doi.org/10.3389/FBIOE.2020.00057.
6. Ming Y, Hasan MF, Tatic-Lucic S, Berdichevsky Y. Micro Three-Dimensional neuronal cultures generate developing Cortex-Like activity patterns. Front Neurosci. 2020;14:1044. https://doi.org/10.3389/FNINS.2020.563905/XML/NLM.
7. D'Aiuto L, Naciri J, Radio N, Tekur S, Clayton D, Apodaca G, Di Maio R, Zhi Y, Dimitrion P, Piazza P, Demers M, Wood J, Chu C, Callio J, McClain L, Yolken R, McNulty J, Kinchington P, Bloom D, Nimgaonkar V. Generation of three-dimensional human neuronal cultures: application to modeling CNS viral infections. Stem Cell Res Ther. 2018;9. https://doi.org/10.1186/S13287-018-0881-6.
8. De Vitis E, Stanzione A, Romano A, Quattrini A, Gigli G, Moroni L, Gervaso F, Polini A. The evolution of Technology-Driven in vitro models for neurodegenerative diseases. Adv Sci. 2024;11. https://doi.org/10.1002/advs.202304989.
9. Tao Y, Zhang SC. Neural subtype specification from human pluripotent stem cells. Cell Stem Cell. 2016;19:573–86. https://doi.org/10.1016/J.STEM.2016.10.015.
10. Dolmetsch R, Geschwind DH. The human brain in a dish: the promise of iPSC-derived neurons. Cell. 2011;145:831–4. https://doi.org/10.1016/J.CELL.2011.05.034.
11. Walters-Shumka JP, Sorrentino S, Nygaard HB, Willerth SM. Recent advances in personalized 3D bioprinted tissue models. MRS Bull. 2023;48:632–42. https://doi.org/10.1557/S43577-023-00551-2/METRICS.
12. Centeno EGZ, Cimarosti H, Bithell A. 2D versus 3D human induced pluripotent stem cell-derived cultures for neurodegenerative disease modelling, Molecular Neurodegeneration 2018 13:1 13 (2018) 1–15. https://doi.org/10.1186/S13024-018-0258-4
13. Liu D, Chen S, Win Naing M. A review of manufacturing capabilities of cell spheroid generation technologies and future development. Biotechnol Bioeng. 2021;118:542–54. https://doi.org/10.1002/BIT.27620.
14. Fennema E, Rivron N, Rouwkema J, van Blitterswijk C, De Boer J. Spheroid culture as a tool for creating 3D complex tissues. Trends Biotechnol. 2013;31:108–15. https://doi.org/10.1016/J.TIBTECH.2012.12.003.
15. Zhou S, Szczesna K, Ochalek A, Kobolák J, Varga E, Nemes C, Chandrasekaran A, Rasmussen M, Cirera S, Hyttel P, Dinnyés A, Freude KK, Avci HX. Neurosphere based differentiation of human IPSC improves astrocyte differentiation. Stem Cells Int. 2016;2016. https://doi.org/10.1155/2016/4937689.
16. Choi YJ, Park JS, Lee SH. Size-controllable networked neurospheres as a 3D neuronal tissue model for alzheimer's disease studies. Biomaterials. 2013;34:2938–46. https://doi.org/10.1016/J.BIOMATERIALS.2013.01.038.
17. Pomeshchik Y, Klementieva O, Gil J, Martinsson I, Hansen MG, de Vries T, Sancho-Balsells A, Russ K, Savchenko E, Collin A, Vaz AR, Bagnoli S, Nacmias B, Rampon C, Sorbi S, Brites D, Marko-Varga G, Kokaia Z, Rezeli M, Gouras GK, Roybon L. Human iPSC-Derived hippocampal spheroids: an innovative tool for stratifying alzheimer disease Patient-Specific cellular phenotypes and developing therapies. Stem Cell Rep. 2020;15:256–73. https://doi.org/10.1016/J.STEMCR.2020.06.001.
18. Lee HK, Velazquez Sanchez C, Chen M, Morin PJ, Wells JM, Hanlon EB, Xia W. Three dimensional human Neuro-Spheroid model of alzheimer's disease based on differentiated induced pluripotent stem cells. PLoS ONE. 2016;11:e0163072. https://doi.org/10.1371/JOURNAL.PONE.0163072.
19. Osaki T, Uzel SGM, Kamm RD. Microphysiological 3D model of amyotrophic lateral sclerosis (ALS) from human iPS-derived muscle cells and optogenetic motor neurons. Sci Adv. 2018;4:5847. https://doi.org/10.1126/SCIADV.AAT5847/SUPPL_FILE/AAT5847_SM.PDF.
20. Osaki T, Uzel SGM, Kamm RD. On-chip 3D neuromuscular model for drug screening and precision medicine in neuromuscular disease. Nat Protocols 2020. 2020;15:2. https://doi.org/10.1038/s41596-019-0248-1.
21. Boutin ME, Strong CE, Van Hese B, Hu X, Itkin Z, Chen YC, LaCroix A, Gordon R, Guicherit O, Carromeu C, Kundu S, Lee E, Ferrer M. A multiparametric calcium signal screening platform using iPSC-derived cortical neural spheroids. SLAS Discov. 2022;27. https://doi.org/10.1016/J.SLASD.2022.01.003.
22. Gopal S, Kwon SJ, Ku B, Lee DW, Kim J, Dordick JS. 3D tumor spheroid microarray for high-throughput, high-content natural killer cell-mediated cytotoxicity. Commun Biology. 2021;4:893. https://doi.org/10.1038/s42003-021-02417-2.
23. R.S. Rathore, S. R Ayyannan, S.K. Mahto, Emerging three-dimensional neuronal culture assays for neurotherapeutics drug discovery, https://Doi.org/10.1080/17460441.2022.2061458 17 (2022) 619–628.
24. Woodruff G, Phillips N, Carromeu C, Guicherit O, White A, Johnson M, Zanella F, Anson B, Lovenberg T, Bonaventure P, Harrington AW. Screening for modulators of neural network activity in 3D human iPSC-derived cortical spheroids. PLoS ONE. 2020;15. https://doi.org/10.1371/JOURNAL.PONE.0240991.
25. Kim SJ, Kim EM, Yamamoto M, Park H, Shin H. Engineering Multi-Cellular spheroids for tissue engineering and regenerative medicine. Adv Healthc Mater. 2020;9. https://doi.org/10.1002/ADHM.202000608.
26. Manzoor AA, Romita L, Hwang DK. A review on microwell and microfluidic geometric array fabrication techniques and its potential applications in cellular studies. Can J Chem Eng. 2021;99:61–96. https://doi.org/10.1002/CJCE.23875.

27. Dahlmann J, Kensah G, Kempf H, Skvorc D, Gawol A, Elliott DA, Dräger G, Zweigerdt R, Martin U, Gruh I. The use of agarose microwells for scalable embryoid body formation and cardiac differentiation of human and murine pluripotent stem cells. Biomaterials. 2013;34:2463–71. https://doi.org/10.1016/J.BIOMATERIALS.2012.12.024.
28. Hsiao C, Palecek SP. Microwell regulation of pluripotent stem cell self-renewal and differentiation. Bionanoscience. 2012;2:266. https://doi.org/10.1007/S12668-012-0050-9.
29. Khademhosseini A, Ferreira L, Blumling J, Yeh J, Karp JM, Fukuda J, Langer R. Co-culture of human embryonic stem cells with murine embryonic fibroblasts on microwell-patterned substrates. Biomaterials. 2006;27:5968–77. https://doi.org/10.1016/J.BIOMATERIALS.2006.06.035.
30. Sen D, Voulgaropoulos A, Keung AJ. Effects of early geometric confinement on the transcriptomic profile of human cerebral organoids. BMC Biotechnol. 2021;21:1–16. https://doi.org/10.1186/S12896-021-00718-2/FIGURES/6.
31. Hwang YS, Bong GC, Ortmann D, Hattori N, Moeller HC, Khademhosseinia A. Microwell-mediated control of embryoid body size regulates embryonic stem cell fate via differential expression of WNT5a and WNT11. Proc Natl Acad Sci U S A. 2009;106:16978–83. https://doi.org/10.1073/PNAS.0905550106.
32. Mohr JC, Zhang J, Azarin SM, Soerens AG, de Pablo JJ, Thomson JA, Lyons GE, Palecek SP, Kamp TJ. The microwell control of embryoid body size in order to regulate cardiac differentiation of human embryonic stem cells. Biomaterials. 2010;31:1885–93. https://doi.org/10.1016/J.BIOMATERIALS.2009.11.033.
33. Ge D, Song K, Guan S, Dai M, Ma X, Liu T, Cui Z. Effect of the neurosphere size on the viability and metabolism of neural stem/progenitor cells. Afr J Biotechnol. 2012;11:3976–85. https://doi.org/10.5897/AJB11.3324.
34. Nelson CM, Jean RP, Tan JL, Liu WF, Sniadecki NJ, Spector AA, Chen CS. Emergent patterns of growth controlled by multicellular form and mechanics. Proc Natl Acad Sci U S A. 2005;102:11594–9. https://doi.org/10.1073/PNAS.0502575102/SUPPL_FILE/02575FIG9.JPG.
35. Campàs O. A toolbox to explore the mechanics of living embryonic tissues. Semin Cell Dev Biol. 2016;55:119. https://doi.org/10.1016/J.SEMCDB.2016.03.011.
36. Bucciarelli A, Paolelli X, De Vitis E, Selicato N, Gervaso F, Gigli G, Moroni L, Polini A. VAT photopolymerization 3D printing optimization of high aspect ratio structures for additive manufacturing of chips towards biomedical applications. Addit Manuf. 2022;60:103200. https://doi.org/10.1016/J.ADDMA.2022.103200.
37. Du ZW, Chen H, Liu H, Lu J, Qian K, Huang CTL, Zhong X, Fan F, Zhang SC. Generation and expansion of highly pure motor neuron progenitors from human pluripotent stem cells. Nat Commun. 2015;6:6626. https://doi.org/10.1038/ncomms7626.
38. Godec P, Pančur M, Ilenič N, Čopar A, Stražar M, Erjavec A, Pretnar A, Demšar J, Starič A, Toplak M, Žagar L, Hartman J, Wang H, Bellazzi R, Petrovič U, Garagna S, Zuccotti M, Park D, Shaulsky G, Zupan B. Democratized image analytics by visual programming through integration of deep models and small-scale machine learning. Nat Commun. 2019;10:4551. https://doi.org/10.1038/s41467-019-12397-x.
39. Jonkman J, Brown CM, Wright GD, Anderson KI, North AJ. Tutorial: guidance for quantitative confocal microscopy. Nat Protoc. 2020;15:1585–611. https://doi.org/10.1038/s41596-020-0313-9.
40. Austria R: A language and environment for statistical computing. R Foundation for Statistical Computing, Vienna, Core Team R. (2017). https://www.r-project.org/ (accessed July 3, 2020).
41. Bucciarelli A, Janigro V, Yang Y, Fredi G, Pegoretti A, Motta A, Maniglio D. A Genipin crosslinked silk fibroin monolith by compression molding with recovering mechanical properties in physiological conditions. Cell Rep Phys Sci. 2021;2:100605. https://doi.org/10.1016/J.XCRP.2021.100605.
42. Bucciarelli A, Olivetti E, Adami A, Lorenzelli L. Design of experiment rational optimization of an inkjet deposition of silver on Kapton. IEEE Sens J. 2021;21:26304–10. https://doi.org/10.1109/JSEN.2021.3058543.
43. Perin F, Spessot E, Famà A, Bucciarelli A, Callone E, Mota C, Motta A, Maniglio D. Modeling a dynamic printability window on polysaccharide blend inks for extrusion Bioprinting. ACS Biomater Sci Eng. 2023;9:1320–31. https://doi.org/10.1021/ACSBIOMATERIALS.2C01143.
44. Aaku-Saraste E, Hellwig A. Huttner loss of occludin and functional tight junctions, but not ZO-1, during neural tube Closure—Remodeling of the neuroepithelium prior to neurogenesis. Dev Biol. 1996;180:664. https://doi.org/10.1006/dbio.1996.0336.
45. Yang M, Liu M, Sánchez YF, Avazzadeh S, Quinlan LR, Liu G, Lu Y, Yang G, O'Brien T, Henshall DC, Hardiman O, Shen S. A novel protocol to derive cervical motor neurons from induced pluripotent stem cells for amyotrophic lateral sclerosis. Stem Cell Rep. 2023;18:1870–83. https://doi.org/10.1016/j.stemcr.2023.07.004.
46. Qu Q, Li D, Louis KR, Li X, Yang H, Sun Q, Crandall SR, Tsang S, Zhou J, Cox CL, Cheng J, Wang F. High-efficiency motor neuron differentiation from human pluripotent stem cells and the function of Islet-1. Nat Commun. 2014;5:3449. https://doi.org/10.1038/ncomms4449.
47. Xu HJ, Yao Y, Yao F, Chen J, Li M, Yang X, Li S, Lu F, Hu P, He S, Peng G, Jing N. Generation of functional posterior spinal motor neurons from hPSCs-derived human spinal cord neural progenitor cells. Cell Regeneration. 2023;12:1–21. https://doi.org/10.1186/S13619-023-00159-6/FIGURES/6.
48. Gong J, Hu S, Huang Z, Hu Y, Wang X, Zhao J, Qian P, Wang C, Sheng J, Lu X, Wei G, Liu D. The requirement of Sox2 for the spinal cord motor neuron development of zebrafish. Front Mol Neurosci. 2020;13:506247. https://doi.org/10.3389/FNMOL.2020.00034.
49. Pasca SP. The rise of three-dimensional human brain cultures. Nat 2018. 2018;553:7689553. https://doi.org/10.1038/nature25032.
50. Razian G, Yu Y, Ungrin M. Production of large numbers of Size-controlled tumor spheroids using microwell plates. J Vis Exp. 2013;50665. https://doi.org/10.3791/50665.
51. Ungrin MD, Joshi C, Nica A, Bauwens C, Zandstra PW. Reproducible, ultra High-Throughput formation of multicellular organization from single cell Suspension-Derived human embryonic stem cell aggregates. PLoS ONE. 2008;3. https://doi.org/10.1371/JOURNAL.PONE.0001565.
52. Lindström S, Hammond M, Brismar H, Andersson-Svahn H, Ahmadian A. PCR amplification and genetic analysis in a microwell cell culturing chip. Lab Chip. 2009;9:3465–71. https://doi.org/10.1039/B912596E.
53. Decarli MC, de Castro MV, Nogueira JA, Nagahara MHT, Westin CB, de Oliveira ALR, da Silva JVL, Moroni L, Mota C, Moraes ÂM. Development of a device useful to reproducibly produce large quantities of viable and uniform stem cell spheroids with controlled diameters. Biomaterials Adv. 2022;135:112685. https://doi.org/10.1016/J.MSEC.2022.112685.
54. Zuchowicz NC, Belgodere JA, Liu Y, Semmes I, Monroe WT, Tiersch TR. Low-Cost Resin 3-D Printing for Rapid Prototyping of Microdevices: Opportunities for Supporting Aquatic Germplasm Repositories, Fishes 2022, Vol. 7, Page 49 7 (2022) 49. https://doi.org/10.3390/FISHES7010049
55. Wang X, Liu J, Zhang Y, Kristiansen PM, Islam A, Gilchrist M, Zhang N. Advances in precision microfabrication through digital light processing: system development, material and applications. Virtual Phys Prototyp. 2023;18. https://doi.org/10.1080/17452759.2023.2248101.
56. Wardwell-Swanson J, Suzuki M, Dowell KG, Bieri M, Thoma EC, Agarkova I, Chiovaro F, Strebel S, Buschmann N, Greve F, Frey O. A framework for optimizing High-Content imaging of 3D models for drug discovery. SLAS Discovery. 2020;25:709–22. https://doi.org/10.1177/2472555220929291.
57. Murphy WL, McDevitt TC, Engler AJ. Materials as stem cell regulators. Nat Mater 2014. 2014;13:6. https://doi.org/10.1038/nmat3937.
58. Thomsen AR, Aldrian C, Bronsert P, Thomann Y, Nanko N, Melin N, Rücker G, Follo M, Grosu AL, Niedermann G, Layer PG, Heselich A, Lund PG. A deep conical agarose microwell array for adhesion independent three-dimensional cell culture and dynamic volume measurement. Lab Chip. 2017;18:179–89. https://doi.org/10.1039/C7LC00832E.
59. Stifani N. Motor neurons and the generation of spinal motor neuron diversity. Front Cell Neurosci. 2014;8:65607. https://doi.org/10.3389/FNCEL.2014.00293.
60. Lee S, Cuvillier JM, Lee B, Shen R, Lee JW, Lee SK. Fusion protein Isl1-Lhx3 specifies motor neuron fate by inducing motor neuron genes and concomitantly suppressing the interneuron programs. Proc Natl Acad Sci U S A. 2012;109:3383–8. https://doi.org/10.1073/PNAS.1114515109.
61. Lee JM, Moon JY, Shaker MR, Sun W, Chung BG. Uniform-sized neurosphere-mediated motoneuron differentiation in microwell arrays. Electrophoresis. 2017;38:3161–7. https://doi.org/10.1002/ELPS.201700118.
62. Mukomoto R, Nashimoto Y, Terai T, Imaizumi T, Hiramoto K, Ino K, Yokokawa R, Miura T, Shiku H. Oxygen consumption rate of tumour spheroids during necrotic-like core formation. Analyst. 2020;145:6342–8. https://doi.org/10.1039/D0AN00979B.
63. Hayashi Y, Ohnuma K, Furue MK. Pluripotent stem cell heterogeneity. Adv Exp Med Biol. 2019;1123:71–94. https://doi.org/10.1007/978-3-030-11096-3_6.

64. Bogacheva MS, Harjumäki R, Flander E, Taalas A, Bystriakova MA, Yliperttula M, Xiang X, Leung AW, Lou YR. Differentiation of human pluripotent stem cells into definitive endoderm cells in various flexible Three-Dimensional cell culture systems: possibilities and limitations. Front Cell Dev Biol. 2021;9:726499. https://doi.org/10.3389/FCELL.2021.726499.

Publisher's note